

Developing Dynamic Ion Transport Channels in Polymer Solid Electrolytes for High-Performance Lithium Metal Batteries

Qiang Lv, Li-an Li, Xi Zhang, Runqi Wang, Ning Wen, Lijuan Xue, Haimei Wang,* Lei Shen, Dairong Chen, Francesco Ciucci, and John Wang



Cite This: *J. Am. Chem. Soc.* 2025, 147, 27611–27623



Read Online

ACCESS |

Metrics & More

Article Recommendations

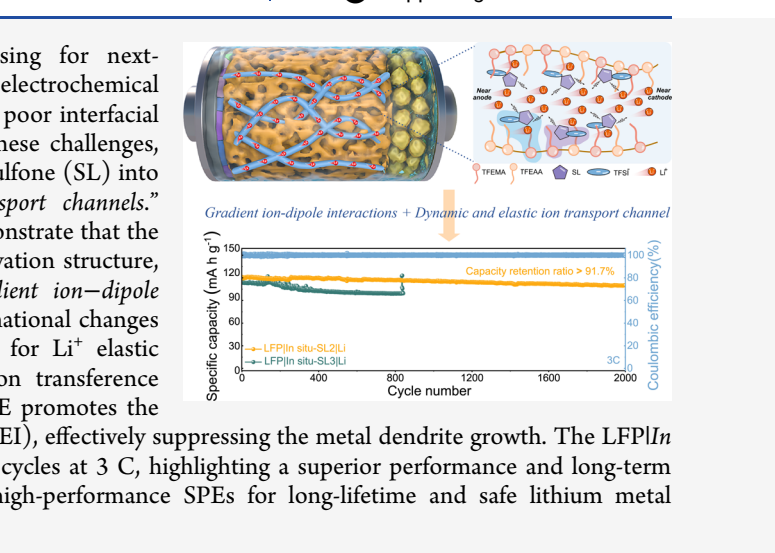
Supporting Information

ABSTRACT: Solid polymer electrolytes (SPEs) are promising for next-generation solid-state lithium metal batteries owing to their electrochemical stability and high safety. However, limited ionic conductivity and poor interfacial stability have hindered their practical applications. To address these challenges, we propose a novel approach by incorporating trace amounts of sulfone (SL) into polyacrylic-based SPEs, purposely creating “dynamic ion transport channels.” Molecular dynamics simulations and experimental validation demonstrate that the optimal incorporation of SL (*in situ*-SL₂) precisely tunes the solvation structure, establishing dense, multipoint coordination networks *via gradient ion-dipole interactions*. The inherent flexibility of SL facilitates rapid conformational changes and dynamic bridging with Li⁺ ions, reducing energy barriers for Li⁺ elastic hopping and thus enhancing ionic conductivity and lithium-ion transference numbers. Detailed interfacial analysis reveals that *in situ* SL₂ SPE promotes the formation of a stable, inorganic-rich solid electrolyte interphase (SEI), effectively suppressing the metal dendrite growth. The LFPI*In situ*-SL₂|Li cell exhibits over 91.7% capacity retention after 2000 cycles at 3 C, highlighting a superior performance and long-term stability. This work provides valuable insights into designing high-performance SPEs for long-lifetime and safe lithium metal batteries.

1. INTRODUCTION

Lithium metal batteries (LMBs) have emerged as a leading candidate for next-generation energy storage systems primarily due to their high theoretical energy density (3860 mAh g⁻¹) and the potential for achieving superior overall performance metrics compared to conventional lithium-ion batteries. However, the widespread commercialization of LMBs is hindered by the flammability of liquid electrolytes and the risks associated with thermal runaway reaction. To address these critical safety issues, solid-state electrolytes (SEs) have gained substantial attention as promising alternatives.^{1–4} Among various SEs, solid polymer electrolytes (SPEs) stand out owing to their advantages related to film processing capabilities and morphological and compositional flexibility.^{5–9}

Despite the considerable advancements, SPEs still face several significant challenges for their practical applications.^{10–12} A primary issue lies in the ion transport within polymer electrolytes, which relies heavily on the mobility of the polymer chain segments.¹³ Several polymers commonly used in SPEs exhibit high glass transition temperatures (T_g), restricting chain movement and resulting in low ionic conductivities (10^{-8} to 10^{-5} S cm⁻¹) at room temperature (RT). Since ion transport in SPEs relies on the segmental motion of polymer chains, lowering T_g creates a transient free volume that enables more efficient Li⁺ hopping between coordination sites.



Additionally, the low degrees of lithium salt dissociation and the strong coordination between lithium ions and polar polymer chains (linked to O-Li⁺ interactions) further reduce lithium-ion mobility, resulting in a low lithium-ion transference number (t_{Li}^+), ranging between 0.2 and 0.5.¹⁴ Moreover, poor electrode/SPE interfacial contact and interfacial compatibility¹⁵ further increase ion transport barriers, raise interfacial impedance, and reduce the cell's efficiency and longevity.

To address these challenges, high-dielectric-constant, organic small molecules, such as dimethyl sulfoxide (DMSO),¹⁶ *N,N*-dimethylformamide (DMF),^{17,18} and *N*-methyl-2-pyrrolidone (NMP),¹⁹ have been used as plasticizers to enhance the performance of SPEs. These small molecules facilitate improved transport kinetics by triggering local solvation conformational adjustments of the polymer matrix, thereby ameliorating the Li⁺ ion transport microenvironment. However, excessive plasticizer additions compromise the mechanical integrity and thermal stability of SPEs. Under

Received: April 8, 2025

Revised: July 14, 2025

Accepted: July 15, 2025

Published: July 24, 2025



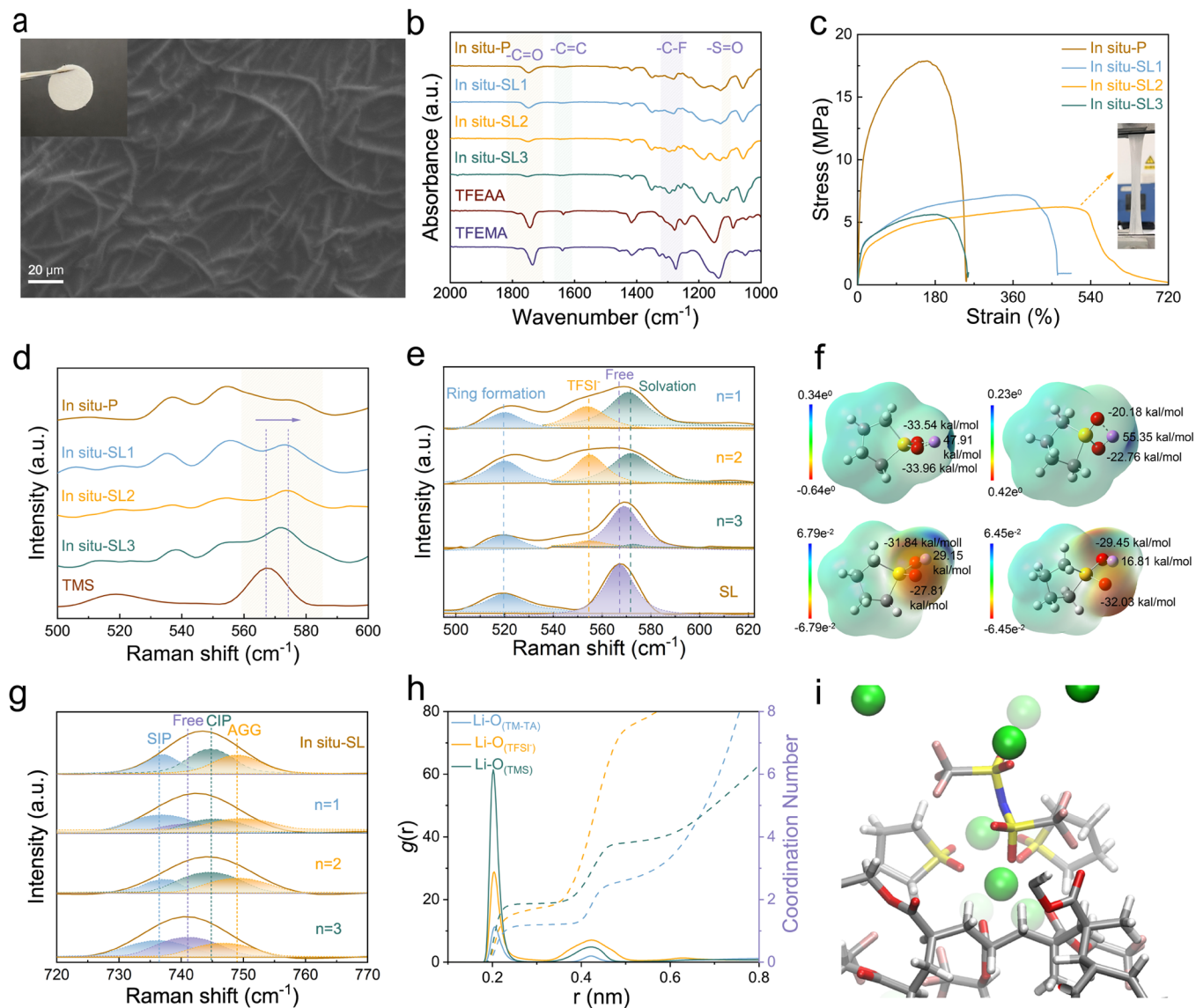


Figure 1. (a) Surface SEM image of the *in situ*-SL2 SPE following polymerization (inset digital photograph). (b) FT-IR spectra of the monomers and polymer matrices. (c) Tensile stress–strain curves and (d) Raman spectra of *in situ*-based SPEs. (e) ^{7}Li NMR spectra. (f) Surface electrostatic potential distribution map changes with the angle and dihedral angle of SL. (g) Lorentzian–Gaussian deconvoluted Raman spectra in the range of 720–770 cm^{-1} . (h) Radial distribution functions ($g(r)$, solid line) and coordination number (dashed line) calculated from MD simulations of *in situ*-SL2 SPE. (i) MD snapshots of *in situ*-SL2 SPE. Color legend: oxygen (yellow), hydrogen (red), carbon (gray), fluorine (white), and lithium (green).

practical operating conditions, these additives suffer from limited electrochemical stability and undergo parasitic reactions with electrodes or electrolytes at high voltage or in harsh chemical environments, resulting in continuous decomposition, a narrowed electrochemical window, interfacial instability, and capacity fading.²⁰ In addition, the underlying molecular-level interactions and the precise ion transport mechanism remain unclear.²¹ Hence, optimizing the concentration of functional additives in SPEs that can establish appropriate ion–dipole interactions and benefit ion transport through solvation conformational changes would be critical for developing high-performance polymer electrolytes that combine high ionic conductivity with robust interfacial stability.^{22,23}

In this study, we developed a poly(acrylic acid)-based electrolyte using a straightforward thermal-initiated *in situ* curing method. The electrolyte was specifically modified with

trace amounts of sulfolane (SL), which was selected for its exceptional oxidative and thermal stability, compatibility with high-voltage batteries, and high relative permittivity (43.38). Molecular dynamics (MD) simulations were conducted to understand the solvation shell and ion transport mechanisms within these polymer electrolytes. By optimizing the SL/LiTFSI molar ratio to form $[\text{Li}^+(\text{SL})_2][\text{TFSI}^-]_n$ aggregated anionic solvent structures (AGG), we established a dense and multiple coordination network governed by *gradient ion–dipole interactions* involving the functional group sites of sulfolane, TFSI^- , and the polymer backbone. Notably, with their low conformational energy barriers by pseudorotation and flexible coordination with Li^+ through the SO_2 crown, sulfolane molecules facilitate rapid conformational rearrangement and orientation adjustment, constructing a *dynamic ion transport channel*. The set of flexibilities enables lithium ions to migrate between adjacent coordination sites *via* a hopping mechanism

independent of large-scale solvent motion or polymer chain relaxation. Accordingly, the flexible ion transport channel significantly increases the lithium-ion transference number (0.87) and ionic conductivity (0.44×10^{-3} S cm $^{-1}$) at room temperature, while reducing concentration polarization at high-voltage electrode interfaces. Further detailed interfacial analysis reveals that *in situ*-SL2 SPE facilitates the formation of a stable, inorganic-rich SEI, which effectively suppresses lithium dendrite growth. Consequently, the LiFePO₄||Li full cell can be cycled stably 2000 times at 3 C for a long period of time, with the capacity retention rate of >91.7%. Overall, this work establishes a molecular-level paradigm for SPE design by incorporating conformationally flexible small molecules to precisely tailor local solvation structures and dynamic Li $^{+}$ transport channels. More broadly, this customizable framework can be extended to diverse SPEs, inspiring the formulation of versatile solid-state electrolytes for next-generation, high-energy-density, long-lifetime batteries.

2. RESULTS AND DISCUSSION

2.1. Structure Design and Characterization. We utilized a straightforward thermally initiated *in situ* curing strategy to fabricate a polyacrylate-based solid polymer electrolyte modulated by trace amounts of sulfolane. The monomers trifluoroethyl acrylate (TFEMA) and 2,2,2-trifluoroethyl acrylate (TFEAA) were designed to copolymerize in conjunction with polyethylene glycol diacrylate (PEGDA) as the cross-linker and LiTFSI as the lithium salt, producing SPEs with varying SL content, labeled as *In situ*-P, *In situ*-SL1, *In situ*-SL2, or *In situ*-SL3. The competitive copolymerization of the dual-monomer (TFEMA/TFEAA) produced a well-balanced elastomeric matrix, combining mechanical robustness with flexibility to suppress metal dendrite growth and stabilize the interface. As illustrated in Figure S1, optical images confirm the successful transition from a flowable liquid precursor to a nonflowable, soft solid, confirming the successful *in situ* polymerization. After polymerization, the polymer matrix was uniformly incorporated into an electrospun PVDF-HFP/HAP membrane with a thickness of approximately 64 μ m (Figures 1a and S2), ensuring smooth surfaces and preventing inhomogeneous lithium deposition.²⁴ Fourier-transform infrared (FT-IR) spectroscopy (Figure 1b) further validates successful polymerization *via* the disappearance of the C=C bond signals at 1630 cm $^{-1}$, indicating the success of the *in situ* curing process. The degree of polymerization (DP) of *in situ*-based SPEs was evaluated by gel permeation chromatography (GPC). The DP values for *in situ*-based SPEs are all around 165–170 (Figure S3 and Table S1), indicating that the incorporation of SL additives does not affect the polymerization of the polymers. As depicted in Figure 1c, mechanical tests demonstrated that *in situ*-SL2 maintained an excellent balance of tensile strength (6.2 MPa) and 532% elongation, indicating its remarkable flexibility, which is critical for buffering volume changes during lithium metal deposition. To evaluate the mechanical durability of the *in situ*-SL2 SPE, cyclic tensile tests up to 100% strain were conducted over 50 cycles (Figure S4). The *in situ*-SL2 membrane retained approximately 87.5% of its maximum stress with negligible plastic deformation and no visible cracks, demonstrating robust elasticity and mechanical resilience during long-term battery cycling. To assess the impact of trace amounts of SL on the crystallinity and thermal stability of the polymer, differential scanning calorimetry

(DSC, Figure S5) was employed, revealing that introducing SL reduces the T_g of the SPE, reflecting higher amorphous content that increases segmental mobility and boosts ionic conductivity. However, excessive liquid additive compromised mechanical strength (Figure 1c).²⁵ In addition, thermogravimetric analysis (TGA) (Figure S6) demonstrates that *in situ*-based SPEs remain thermally stable up to 300 °C (weight loss <20%), with only a slight reduction in thermal retention when SL content increases. Flame-resistance tests (Figure S7) demonstrate that the PVDF-HFP/HAP membrane backbone confers inherent flame resistance, primarily due to the incorporation of hydroxyapatite (HAP) with its high melting point and low thermal conductivity.^{26,27} Additionally, the incorporated SL exhibits low flammability,²⁸ ensuring that *in situ*-SL2 maintains its shape and size under flame exposure and could self-extinguish with minimal structural change. Ultimately, the moderate SL content in *in situ*-SL2 SPE not only enhances mechanical flexibility but also maintains desirable thermal stability and flame resistance, making it well-suited for safe and high-performance lithium–metal batteries.

The local solvation conformation in polymer electrolytes is also pivotal for Li $^{+}$ transport microenvironments and interfacial chemistry.^{29,30} As shown in Figures 1d and S8, incorporating [Li $^{+}$ (SL)₂][TFSI $^{-}$]_n into the *in situ*-cured polymer framework significantly alters the SO₂ scissoring vibration around 568 cm $^{-1}$ in SL and shifting to higher wavenumbers, reflecting multiple coordination modes (i.e., monodentate or bridging) within *in situ*-SL2 SPE.³¹ Furthermore, ⁷Li solid-state NMR (Figure 1e) reveals that, compared to the *in situ*-P and *in situ*-SL1 SPEs, *in situ*-SL2 SPE exhibits a downfield shift of the ⁷Li peak from -0.31 to -0.07, indicating weakened shielding and enhanced salt dissociation, contributing to increased Li $^{+}$ conductivity.³² Although *in situ*-SL3 displays a further downfield shift (0.016 ppm) relative to *in situ*-SL2 SPE, the excessive SL content disrupts the optimized aggregated solvation structure and ion transport channels, ultimately yielding a lower Li $^{+}$ transference number than that of *in situ*-SL2 SPE.

The analysis of the surface electrostatic potential distribution map (Figure 1f) further reveals that SL, which possesses dual coordinating sites, displays a significant electronegativity on its donor oxygen atoms, enabling it to bridge multiple Li $^{+}$ ions.³³ As SL undergoes conformational changes, including variations in bond angles and dihedral angles, its coordination with Li $^{+}$ ions could demonstrate either symmetrical or asymmetrical binding configurations. The varying electronegativities at the polar sites of TFEMA–TFEAA polymer chains, TFSI $^{-}$ anions, and SL molecules (Figure S9), combined with the conformational flexibility of SL, generate gradient ion–dipole interactions with Li $^{+}$ ions. Consistent with the Raman results, these solvent-bridged coordination network structures and gradient interaction sites establish a ligand-channel architecture, enabling Li $^{+}$ ions' elastic "hopping" among various coordination sites, ultimately enhancing Li $^{+}$ conduction.³⁴ To characterize the solvation structure more precisely, we applied Lorentzian–Gaussian peak fitting for the Raman spectra presented in Figures 1g and S8.³⁵ This method integrates the features of Lorentzian and Gaussian functions, capturing natural line width and instrumental broadening, allowing for accurate deconvolution of overlapping peaks. In the 540–620 cm $^{-1}$ region, the SO₂ scissoring vibration of SL broadens and shifts in response to various Li $^{+}$ coordination states.³¹ Meanwhile, the 720–760 cm $^{-1}$ region could be assigned to

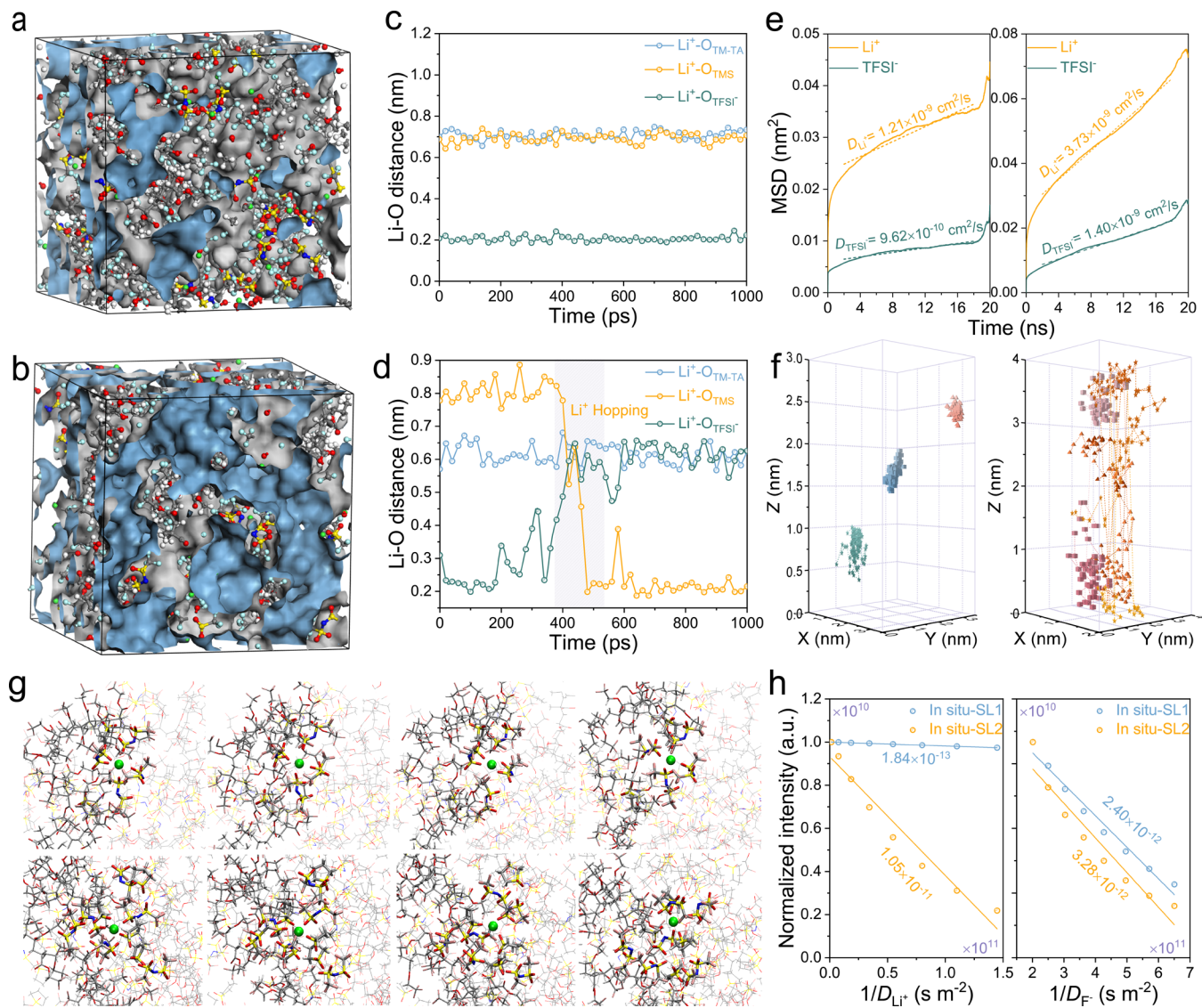


Figure 2. Density field diagram illustrating lithium-ion transport channels for (a) *in situ*-SL1 SPE and (b) *in situ*-SL2 SPE. Internuclear distances between a Li⁺ and representative O atoms in the inner solvation shell of (c) *in situ*-SL1 SPE and (d) *in situ*-SL2 SPE. (e) Mean square displacement (MSD) of Li⁺ and (f) 3D trajectory of representative Li⁺ ions in *in situ*-SL1 SPE (left) and *in situ*-SL2 SPE (right). (g) Chronological snapshots depicting the movement of a specific lithium atom in *in situ*-SL1 (top) and *in situ*-SL2 SPE (bottom). (h) PFG-echo intensity as a function of the squared gradient amplitude from the ⁷Li and ¹⁹F PFG-NMR experiment of *in situ*-SL1 SPE and *in situ*-SL2 SPE.

–CF₃ bending coupled with the S–N–S stretching vibration in TFSI[–]. As shown in Figure 1g, TFSI[–] primarily exists as contact ion pairs (CIPs) and aggregate coordinations (AGGs) in the *in situ*-SL2 electrolyte (at \sim 745–750 cm^{–1}), effectively reducing free anions (at \sim 741 cm^{–1}). This suggests the formation of polyanionic solvation structures, elevating the lithium-ion transference number by immobilizing TFSI[–] and releasing more Li⁺ for conduction.^{36,37} Molecular dynamics simulations further clarify these solvation environments by calculating radial distribution functions (RDFs) around Li⁺.^{38,39} Integrating the first RDF peak (within \sim 2 Å) yields coordination numbers of 2.72 (O-SL) and 2.66 (O-TFSI[–]) in the *in situ*-SL2 SPE (Figure 1h), indicating the average sulfolane- and TFSI[–]-derived oxygen atoms coordinating each Li⁺ within its first solvation shell, which underpins the AGG solvation structure and anion-derived inorganic-rich SEI components.⁴⁰ Moreover, the corresponding snapshots of MD simulation (Figures 1i and S11) depict Li⁺ ions

surrounded by polymer (C=O groups), SL (S=O groups), and TFSI[–] (O=S=O groups), establishing gradient ion–dipole interactions and a solvation network, which are crucial for enhancing Li⁺ transport efficiency and interfacial stability in solid-state batteries.

2.2. Ion Coordination and Kinetic Transport Mechanism. To comprehensively understand the ion transport mechanisms within the polymer electrolyte containing trace amounts of SL, we have constructed structural models and performed MD simulations.⁴¹ By comparing the polymer electrolyte lacking SL of *in situ*-SL1 (Figure 2a) with the optimized SL addition in *in situ*-SL2 (Figure 2b), the blue regions show a significant enhancement in the number of ion-transporting channels, attributing to the regulation of the solvation environment and the formation of dense, multipoint coordination networks by SL.⁴² Specifically, these well-linked networks arise from gradient ion–dipole interactions among Li⁺, SL (S=O), and either polymer (C=O) or TFSI[–] (O=

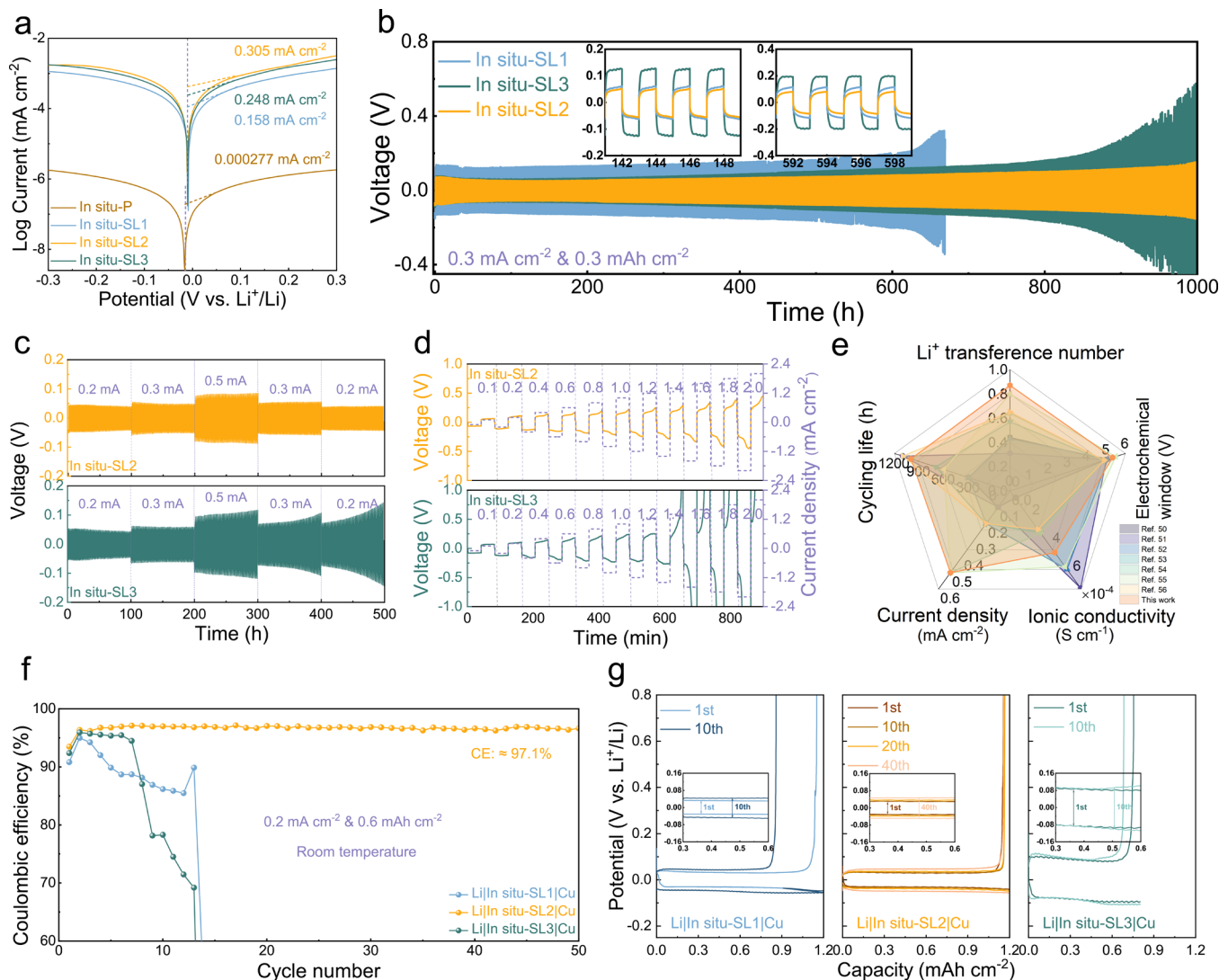


Figure 3. (a) Ionic conductivity and (b) Nyquist curve of the electrochemical impedance spectroscopy (EIS) test at RT. (c) Activation energy fitted with Arrhenius models. (d) LSV curves at RT with the voltage sweeping rate of 0.1 mV s^{-1} . Steady-state chronoamperometry polarization curves under 10 mV polarization voltage of (e) *in situ*-SL2 and (f) *in situ*-SL3 SPE. (g) EIS Nyquist plots of Li-symmetric batteries with different *in situ*-based SPEs, respectively. (h) Schematic diagram of the ion transport mechanism in *in situ*-SL2 SPE.

$\text{S}=\text{O}$) groups, resulting in the formation of $[\text{Li}^+(\text{SL})_2] \cdot [\text{TFSI}^-]_n$ units that create numerous pathways for Li^+ ion hopping. Trajectory analysis supports the hypothesis of the hopping diffusion mechanism.⁴³ Figure 2c,d presents the Li^+ Cartesian coordinates as a function of time, revealing frequent Li^+ hopping between adjacent sites within this dynamic coordination framework in *in situ*-SL2. During this process, Li^+ ions dissociate from TFSI^- and interact with $\text{S}=\text{O}$ groups of SL to achieve swift migration, decoupled from the limited segmental motion of polymer chains.

Mean square displacement (MSD) analysis was used to calculate the diffusion coefficients by fitting the long-time linear regime of the MSD curves according to the Einstein relation.⁴⁴ The 3D trajectories of representative Li^+ ions in *in situ*-SL2 (Figure 2f) demonstrate significantly increased dynamic activity and more continuous migration paths compared to *in situ*-SL1, indicating wider migration ranges and improved mobility.^{45,46} These findings suggest that the introduction of an optimal amount of SL can create a robust, dense, and flexible coordination network with multiple elastic

hopping pathways, therefore reducing energy barriers for Li^+ transport and accelerating ion conduction. Consequently, the optimized solvation structure and dynamic channel not only enhance the ionic conductivity and transference number but also mitigate concentration polarization, thereby improving the overall performance and stability of the solid-state lithium metal batteries.

To further visualize the Li^+ transport pathway, chronological snapshots from the MD simulations (Figure 2g) clearly illustrate the movement of a specific lithium atom in the *in situ*-SL2 system.^{34,47} Lithium ions “hop” via frequently exchange coordination sites within the densely packed AGG solvation structures, while SL molecules dynamically rotate and flexibly switch their conformation without disrupting the conduction network. This dynamic coordination ensures that the conduction network remains intact and flexible, providing an adaptable environment that allows Li^+ to travel efficiently without being tightly bound. In contrast, Li^+ ions become trapped by the TFSI^- anions in the systems with insufficient SL, which results in restricted movement and slower migration.

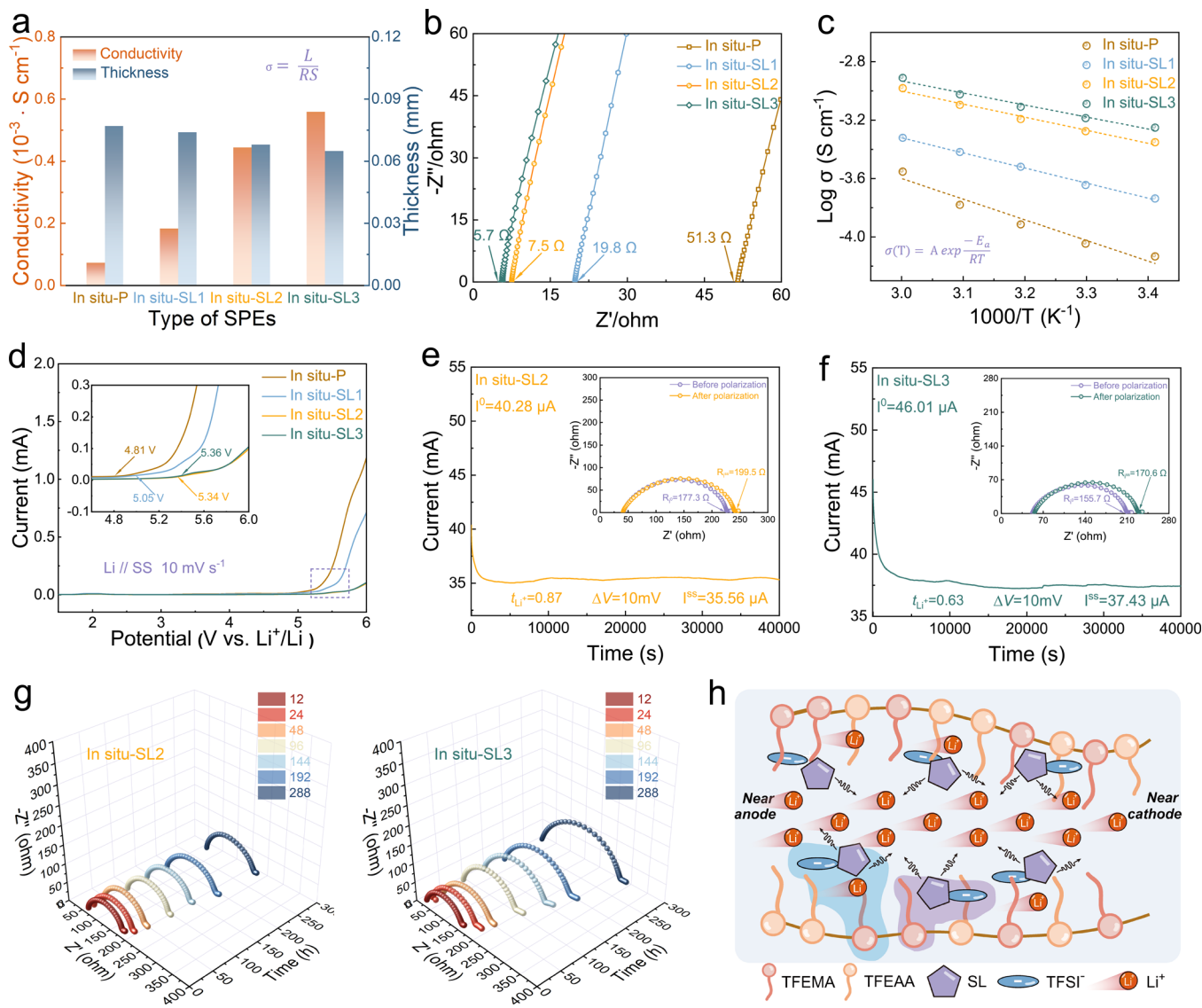


Figure 4. (a) Tafel plots of Li-symmetric cells assembled with *in situ*-based SPEs. (b) Galvanostatic cycling curves at 0.3 mA cm^{-2} and 0.3 mAh cm^{-2} . The inset shows enlarged curves at 140–150 and 590–600 h. (c) Constant current polarization curves at various current densities. (d) Critical current density (CCD) test under step-up current densities (0.1 – 2.0 mA cm^{-2}) with a consistent plating/stripping time of 1 h of Li||*In situ*-SL2||Li and Li||*In situ*-SL3||Li batteries. (e) Performance comparison of SPEs based on the *in situ*-SL2 SPE in this study with polymer electrolytes from recent publications. (f) Performance of Cu||Li half cells using *in situ*-based SPEs at 0.2 mA cm^{-2} and 0.6 mAh cm^{-2} . (g) Voltage–capacity profiles of lithium plating/stripping in Cu||Li half cells with *in situ*-based SPEs.

In addition, pulse field gradient nuclear magnetic resonance (PFG-NMR) diffusometry further supports the MD simulation findings by providing direct evidence of the ion mobility and diffusion dynamics in the electrolyte.⁴⁸ Here, ⁷Li NMR probes Li⁺ transport, while ¹⁹F NMR measures the mobility of the TFSI⁻ anions. The respective self-diffusion coefficients for both Li⁺ (D_{Li^+}) and TFSI⁻ (D_{TFSI^-}) were extracted by fitting the signal attenuation to the Stejskal–Tanner equation. As shown in Figure 2h, PFG-NMR demonstrates the rapid migration of Li⁺ ions and slower anion migration in the *in situ*-SL2 SPE, suggesting that the anions are limited by the solvation network within the polymer chains. This selective ion transport behavior aligns with the hypothesis of the complete dissociation of Li⁺ ions and enhances the lithium-ion diffusion coefficients. As a result, Li⁺ ions migrate rapidly through the dynamic ion-conductive network *via* a ligand-exchange/hopping mechanism.³¹ The combination of MD and PFG-

NMR reveals the fundamental mechanisms underlying lithium-ion hopping and transport in SL-regulated SPEs.

2.3. Electrochemical Properties of *In Situ*-Based SPEs.

To thoroughly evaluate the electrochemical performance of the *in situ*-based SPEs, we analyzed the ionic conductivity (σ) of SPEs, which is crucial for governing ion diffusion kinetics during charge/discharge, using asymmetric coin cells with stainless steel electrodes.^{49,50} As illustrated in Figure 3a,b, the addition of sulfolane significantly improves ionic conductivity at room temperature by both increasing the amorphous fraction of the polymer matrix and promoting LiTFSI dissociation. Compared to *in situ*-P and *in situ*-SL1 SPEs, the moderate addition of SL in *in situ*-SL2 raises the ionic conductivity at room temperature to $0.44 \times 10^{-3} \text{ S cm}^{-1}$, while lowering the activation energy from 0.301 eV (*in situ*-P) to 0.189 eV (Figure 3c). This indicates that dynamic ion–dipole interactions and rapid reorientation of SL molecules reduce

energy barriers for Li^+ hopping, thereby enabling faster Li^+ movement through a closely packed, elastic conduction network in the polymer matrix. In addition to improved conductivity, an optimal SL concentration significantly expands the electrochemical stability window from 4.81 to 5.34 V, as verified by linear sweep voltammetry (LSV, Figure 3d). This widened potential range directly results from SL's intrinsic high-voltage tolerance and superior oxidative resistance. The expanded electrochemical window consequently makes these SPEs particularly well-suited for integration with high-voltage cathode materials, which is essential for increasing the energy density.

Furthermore, the lithium-ion transference number (t_{Li^+}) is a key indicator for quantifying the fraction of total ionic conductivity contributed by Li^+ ions.⁵¹ The t_{Li^+} improves significantly to 0.87 in *in situ*-SL2 (Figures 3e,f and S12), indicating that its AGG anion structure and elastic ion channels supply effectively dissociated Li^+ and support a "hopping" conduction mechanism. This mechanism reduces concentration polarization while raising both the conductivity and transference number. Conversely, excessive SL in *in situ*-SL3 slightly increases the macroscopic ionic conductivity but disrupts or loosens the AGG network, favoring a solvent-vehicular transport pathway that drags anions alongside Li^+ , reducing the transference number t_{Li^+} to 0.63. This implies that Li^+ mobility is hindered by anion drag and insufficiently stable coordination pathways.⁵² In addition, the interfacial contact quality and compatibility are evaluated in Li-symmetric cells *via* Nyquist plots under different rest periods (Figures 3g and S13).⁵³ With appropriate SL incorporation, the polymer exhibits a lower interfacial impedance, contributing to the enhanced flexibility that ensures tighter electrode/electrolyte contact. Cross-sectional SEM imaging (Figure S14) further confirms a continuous, void-free interface between the *in situ*-SL2 SPE and lithium metal, further supporting the intimate contact achieved through optimized SL incorporation. After 288 h of rest, the impedance of the *in situ*-SL2 cell remains stable at around 220Ω (compared to its initial 185Ω), reflecting efficient Li^+ transport, reduced ion accumulation at interfaces, and the formation of robust SEI/CEI layers in the *in situ*-SL2 cells. In contrast, electrolytes lacking the appropriate SL concentration suffer from larger polarization, higher interfacial impedance, and compromised long-term performance. As illustrated in Figure 3h, the ion transport mechanism in the *in situ*-SL2 SPE is primarily driven by the dynamic and elastic ion transport channel based on the incorporation of trace amounts of SL, which create multiple pathways facilitating Li^+ ions hopping between adjacent coordination sites. This mechanism leads to improved ionic conductivity, higher lithium-ion transference numbers, and mitigated concentration polarization, thereby enhancing the overall performance and stability of the solid-state electrolyte.

2.4. Electrochemical Performance of Li-Symmetric Battery. To evaluate the reversibility of the lithium plating/stripping process and the interfacial properties between the *in situ*-based SPEs and lithium metal anode, the Li-symmetric cells were assembled. The Tafel plots of symmetric $\text{Li}|\text{Li}$ cells (Figure 4a) reveal that the *in situ*-SL2 cell exhibits a higher exchange current density (i_0) of 0.305 mA cm^{-2} compared to 0.158 mA cm^{-2} for the *in situ*-SL cell, indicating significantly improved charge transfer kinetics, reduced interfacial resistance, and enhanced lithium-ion transport efficiency. As shown in Figure 4b, $\text{Li}|\text{In situ}-\text{SL2}|\text{Li}$ cell exhibits exceptionally stable

cycling for over 1000 h, maintaining an overpotential consistently below 0.16 V, highlighting the mechanical resilience and chemical stability of the *in situ*-SL2 SPE. In contrast, the $\text{Li}|\text{In situ-P}|\text{Li}$ cell exhibited extremely high polarization ($>3 \text{ V}$), primarily due to the poor ionic conductivity of the *In situ*-P SPE without SL additives (Figure S15). Additionally, the $\text{Li}|\text{In situ-SL1}|\text{Li}$ cell experiences a sharp increase in overpotential to 0.34 V after just 665 h, suggesting inferior interfacial compatibility lacking SL. Further rate-performance tests (Figures 4c and S16) reveal that Li-symmetric cells with *in situ*-SL2 sustain lower overpotentials without significant voltage fluctuations across various current densities, reflecting that an optimal amount of SL addition fosters a robust and highly conductive interface, facilitating rapid Li^+ diffusion and uniform plating/stripping. In contrast, $\text{Li}|\text{In situ-SL3}|\text{Li}$ experienced a gradual increase in voltage, implying heightened polarization attributed to inhomogeneous interfaces and large interfacial impedance.

To further quantify the resistance to lithium dendrite growth, a critical current density (CCD) test (Figures 4d and S17) was conducted with stepwise increments in current density ($0.1\text{--}2.0 \text{ mA cm}^{-2}$) for 40 min at each step. The $\text{Li}|\text{In situ-SL2}|\text{Li}$ cell withstands up to 2.0 mA cm^{-2} without short-circuiting, while the $\text{Li}|\text{In situ-SL3}|\text{Li}$ cell failed at 1.4 mA cm^{-2} , highlighting the superior dendrite suppression capability of *in situ*-SL2. Additionally, at a constant current density of 0.1 mA cm^{-2} , the $\text{Li}|\text{In situ-SL2}|\text{Li}$ cell shows stable cycling for over 90 h (Figure S18), corresponding to a cumulative lithium deposition of 9 mAh cm^{-2} ($0.1 \text{ mA cm}^{-2} \times 90 \text{ h}$), whereas the $\text{Li}|\text{In situ-SL3}|\text{Li}$ cell experiences a sharp voltage collapse after only 40 h, indicating short-circuit failure due to uneven lithium deposition and dendrite growth. The excessive sulfolane in the *in situ*-SL3 SPE promotes side reactions and uneven SEI thickening, creating local hotspots where lithium dendrites penetrate the separator.

Notably, even at higher current and capacity densities (e.g., 0.5 mA cm^{-2} and 0.5 mAh cm^{-2}), the $\text{Li}|\text{In situ-SL2}|\text{Li}$ cell can maintain low overpotential and excellent reversibility over 500 plating and stripping cycles (Figure S19). This performance is attributed to rapid Li^+ hopping and exchange conduction through SL-bridged, chain-like coordination networks, which enhance transport properties and minimize interfacial degradation. Compared with prior polymer electrolytes reported in recent publications, the *in situ*-SL2 exhibits competitive performance (Figure 4e),^{54–60} by combining high ionic conductivity with a lithium-ion transference number. This synergy effectively reduces electric field and concentration polarization, minimizes interfacial byproducts, and enables a dense, fast Li^+ conducting SEI at the lithium metal interface, which leads to a lower interfacial resistance and a uniform Li^+ flux. Further evidence for the significance of tuning SL content arises from $\text{Cu}|\text{Li}$ cells. As shown in Figure 4f, the $\text{Cu}|\text{In situ-SL2}|\text{Li}$ cell maintains an average Coulombic efficiency (CE) of 97.1% for 50 cycles at 0.2 mA cm^{-2} and 0.6 mAh cm^{-2} , surpassing both the *in situ*-SL1 SPE and *in situ*-SL3 SPE. Correspondingly, lower lithium plating overpotentials are observed (see Figure 4g), emphasizing the uniform lithium deposition facilitated by the *in situ*-SL2 SPE.

2.5. Electrochemical Performance of Assembled $\text{LiFePO}_4||\text{Li}$ and $\text{NCM}||\text{Li}$ Batteries. To further verify the practical feasibility of the *in situ*-based SPEs, galvanostatic cycling tests were conducted on $\text{LiFePO}_4|\text{SPE}|\text{Li}$ solid-state lithium metal batteries. As shown in Figure 5a, the $\text{LiFePO}_4|\text{In situ-SL2}|\text{Li}$ cell

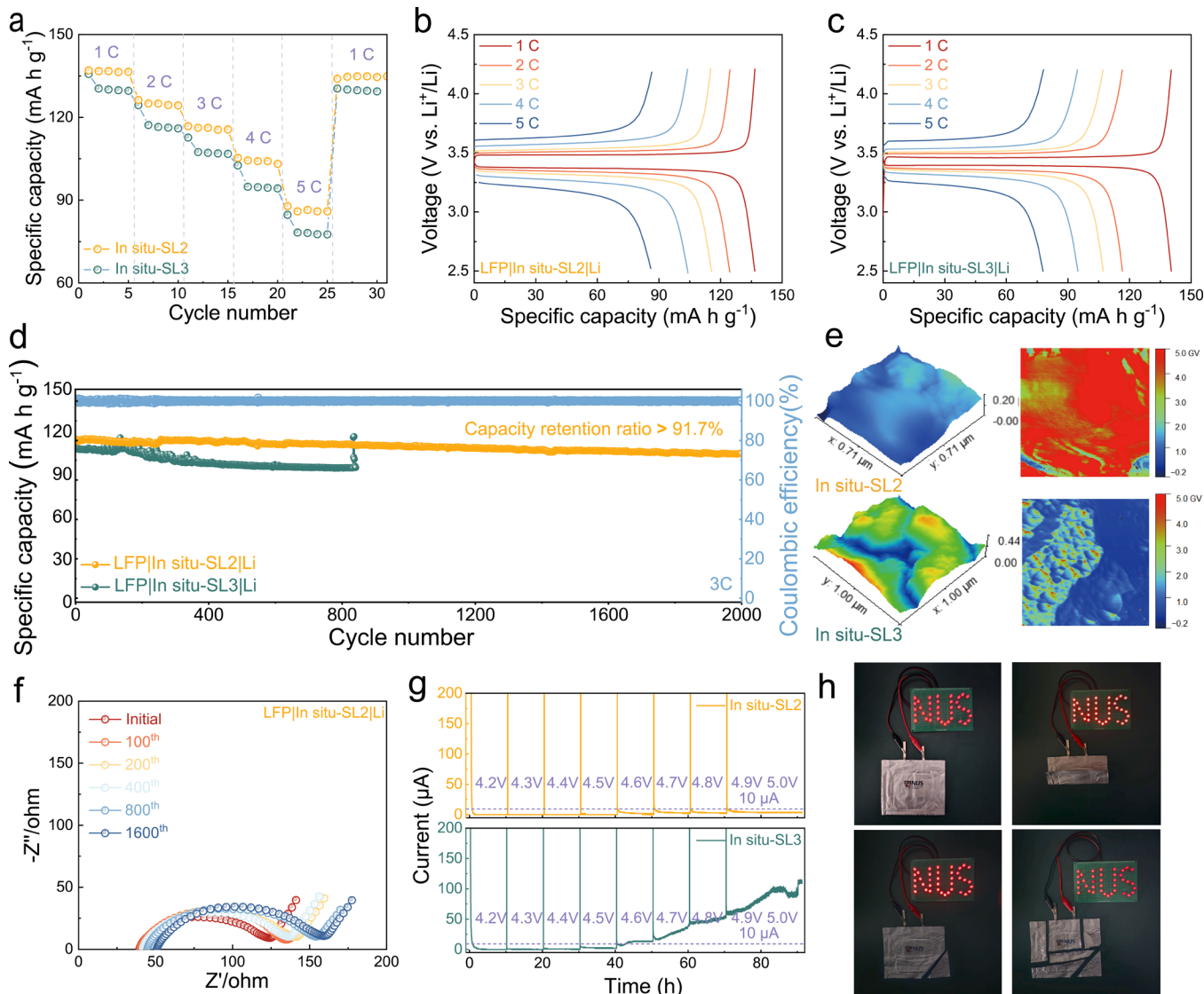


Figure 5. (a) Rate performance of the LFP||*In situ*-SL2||Li and LFP||*In situ*-SL3||Li cells at different C-rates; charge/discharge profiles at various rates for (b) the LFP||*In situ*-SL2||Li cell and (c) the LFP||*In situ*-SL3||Li cells. (d) Long-term cycling performance of LFP||Li cells assembled with different electrolytes at 3 C. (e) AFM image of the roughness and the corresponding Young's modulus distribution patterns of lithium metal after cycling in LFP||*In situ*-SL2||Li cells. (f) EIS Nyquist plots of LFP||*In situ*-SL2||Li cells during cycling. (g) Electrochemical floating analysis of LFP||*In situ*-SL2||Li and LFP||*In situ*-SL3||Li cells from 4.2 to 5.0 V. (h) Safety test of the pouch cell by lighting an LED under bending and cutting conditions.

exhibits superior rate performance compared to the LFP||*In situ*-SL3||Li cell, delivering higher discharge capacities of 136.7, 125.1, 116.2, 105.6, and 87.9 mAh g⁻¹ at rates of 1, 2, 3, 4, and 5 C, respectively, and recovers to 134.8 mAh g⁻¹ when returning to 1 C, which corresponds to 98.6% capacity retention. In contrast, the LFP||*In situ*-SL3||Li demonstrates, respectively, lower capacities of 130.5, 116.5, 107.2, 94.8, and 78.2 mAh g⁻¹ at the same rates. The charge/discharge profiles in Figure 5b, c further confirm the outstanding rate performance of the LFP||*In situ*-SL2||Li cell, attributable to the optimally balanced solvation structure and dynamic Li⁺ transport channels in the *in situ*-SL2 SPE, which support rapid and selective Li⁺ conduction under high-rate conditions.

As illustrated in Figure 5d, the long-term cycling performance tests at 3 C show that LFP||*In situ*-SL2||Li retains a capacity of 104.8 mAh g⁻¹ after 2000 cycles, corresponding to >91.7% capacity retention and 99.9% in Coulombic efficiency, which is superior to the performance previously reported (Table S2).

This excellent stability indicates that the improved Li⁺ transport kinetics and higher t_{Li^+} in the *in situ*-SL2 SPE promote uniform lithium plating/stripping and efficient insertion/extraction at the LFP cathode, thereby mitigating concentration polarization and maintaining cathode utilization even under rapid charge–discharge conditions. In contrast, the LFP||*In situ*-SL3||Li cell experiences significant capacity decay, dropping below 95 mAh g⁻¹ after 800 cycles and eventually exhibiting short-circuit failures due to sluggish Li⁺ kinetics and uneven lithium plating and stripping, leading to dendrite-induced internal failures. Furthermore, the surface roughness of the lithium surface obtained from the atomic force microscope (AFM) in Figure 5e reveals that the SEI formed by *in situ*-SL2 SPE has a higher Young's modulus and lower surface roughness compared to that formed by the *in situ*-SL3 SPE.⁶¹ The enhanced SEI quality, combined with improved Li⁺ transport in *in situ*-SL2 SPE, reduces local hotspots of current density, enabling more uniform lithium plating and stripping

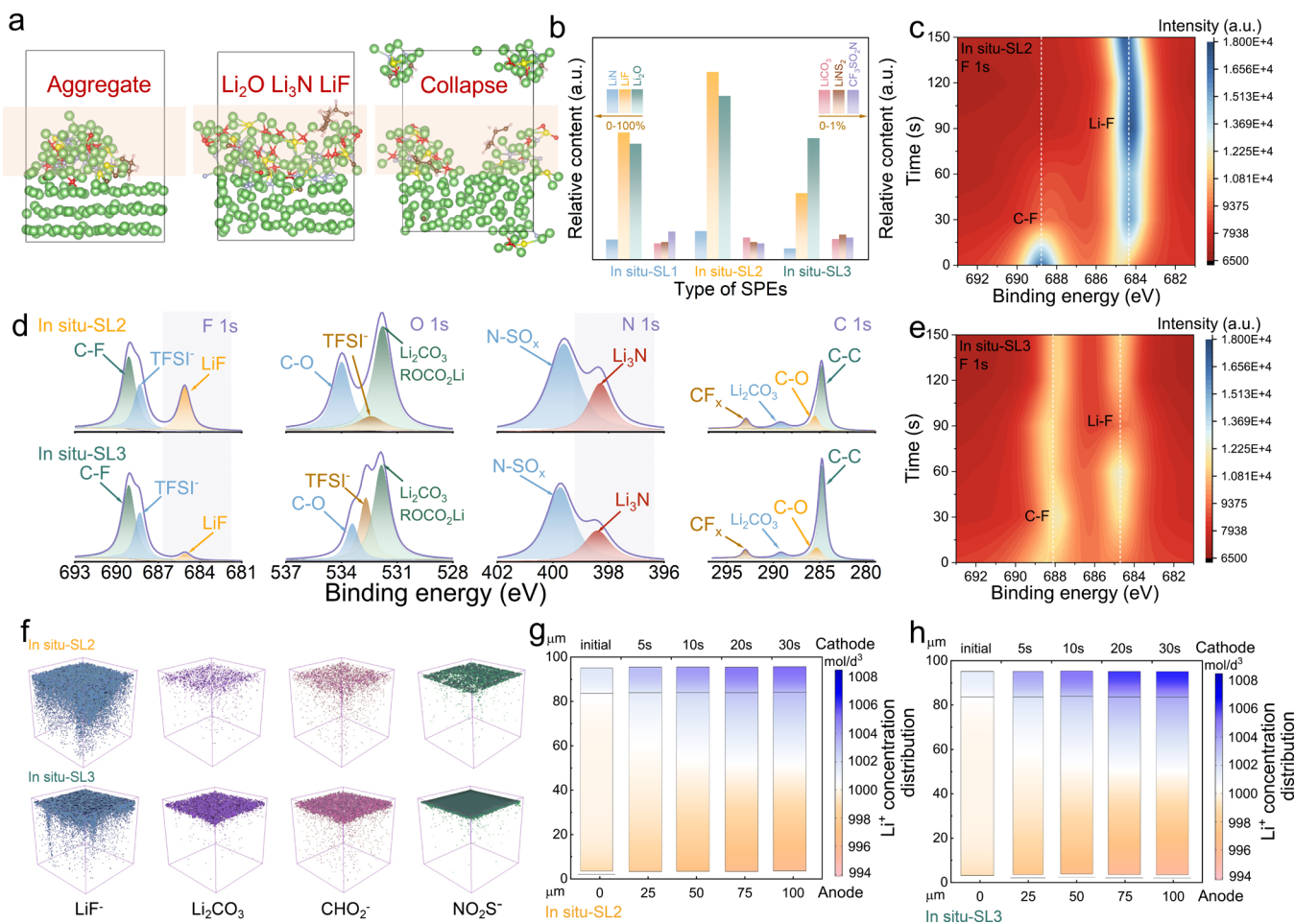


Figure 6. (a) *Ab initio* molecular dynamics (AIMD) simulations of interface reaction and SEI formation of the *in situ*-based electrolytes on lithium metal. (b) Relative contents of the main products in SEI. (c) Elemental analysis and (d, e) depth profiles of F 1s of the lithium surface from cycled $\text{LFPI}|In situ\text{-SL2}|Li$ and $\text{LFPI}|In situ\text{-SL3}|Li$ cells. (f) 3D TOF-SIMS mappings of $\text{LFPI}|In situ\text{-SL2}|Li$ and $\text{LFPI}|In situ\text{-SL3}|Li$ cells after 10 cycles. COMSOL Multiphysics finite-element method (FEMS) simulation of the Li^+ concentration distribution based on (g) $\text{LFPI}|In situ\text{-SL2}|Li$ and (h) $\text{LFPI}|In situ\text{-SL3}|Li$ cells.

on the anode, while effectively suppressing dendrite growth that can result in internal short-circuits and catastrophic capacity loss.

Cyclic voltammetric (CV) curves of the $\text{LFPI}|In situ\text{-SL2}|Li$ cell (Figure S20) exhibited well-overlapping curves over 15 cycles, with an anodic peak at 3.81 V and a cathodic peak at 3.19 V, corresponding to the LiFePO_4 redox reaction with minimal side reactions. This indicates lower potential polarization and superior electrochemical stability compared with the $\text{LFPI}|In situ\text{-SL3}|Li$ cell. As illustrated in Figures S5 and S20, electrochemical impedance analysis further demonstrates that after 1600 cycles, the $\text{LFPI}|In situ\text{-SL2}|Li$ cell retains a lower and more stable interfacial resistance ($\sim 107 \Omega$) compared to the higher resistance observed in the $\text{LFPI}|In situ\text{-SL3}|Li$ cell, indicating improved interfacial compatibility and reduced polarization.

To further explore the high-voltage stability of the *in situ*-based SPEs, we recorded leakage currents at 4.2–5.0 V by conducting electrochemical float tests. As illustrated in Figure S5g, the $\text{LFPI}|In situ\text{-SL2}|Li$ cells quickly returned to a steady state at various step voltages, maintaining a low steady-state leakage current of 10 μA even at 5.0 V. This indicates the minimal polymer or electrolyte decomposition, which contributes to the well-connected ion transport network that

redistributes Li^+ ions to achieve equilibrium at elevated voltages. In contrast, the *in situ*-SL3 cell featuring excess SL had higher leakage currents ($>100 \mu\text{A}$), likely due to solvent oxidation and unstable SEI.

In addition, the combination of the electrolyte with the high-voltage NCM cathode was investigated through galvanostatic cycling tests. As illustrated in Figure S21, the $\text{NCM}|In situ\text{-SL2}|Li$ cell delivers impressive discharge capacities and excellent capacity retention at various rates, reflecting efficient Li^+ ion transport and minimal interfacial degradation. The $\text{NCM}|In situ\text{-SL2}|Li$ cell delivered an initial discharge capacity of 155.6 mAh g^{-1} and retained 80.7% of this capacity after 200 cycles at 0.5 C, further demonstrating sustainable electrochemical characteristics and interfacial stability during high-voltage cycling (Figure S22). Our previous reports indicated that introducing SL enables preferential adsorption at the cathode interface, facilitating the formation of a stable inorganic-rich cathode–electrolyte interface (CEI).⁶² As depicted in Figure S23, the cycled $\text{NCM}|In situ\text{-SL2}|Li$ cell shows less content of $\text{Li}_2\text{CO}_3/\text{ROCO}_2\text{Li}$ and an increased amount of LiF along with more Li_2SO_4 . The uniform and continuous LiF phase accelerates Li^+ transport, while the increased Li_2SO_4 with high oxidative stability effectively suppresses side reactions at

the electrode/electrolyte interface and inhibits the migration of transition metal ions into the CEI layer.⁶³

Finally, the LFP|*In situ*-SL2|Li pouch cell exhibited exceptional mechanical resilience and safety, remaining operational after severe folding and cutting tests (Figure 5h), which highlights the practical feasibility of the *in situ*-SL2 SPE for reliable high-performance battery applications.

2.6. Interfacial Compatibility Evaluation. To gain deeper insights into the interfacial reactions and SEI formation on lithium metal electrodes in *in situ*-based SPEs, *ab initio* molecular dynamics simulations were performed (Figures 6a,b and S24). After 100 ps of AIMD simulation, the *in situ*-SL1 SPE showed incomplete decomposition of TFSI⁻ anions, resulting in the formation of small amounts of LiF, and Li₃N, with Li₂O clustering into aggregates consistent with SEM observations (Figure S25). This indicates heterogeneous nucleation and severe mossy lithium dendrite growth.⁶⁴ The *in situ*-SL3 SPE experiences surface degradation of the lithium metal, indicative of an unstable SEI attributed to the overdecomposition of excess SL. Notably, the *in situ*-SL2 SPE favors the formation of a homogeneous SEI with higher inorganic content (e.g., LiF, Li₃N), as further validated by depth-profiling X-ray photoelectron spectroscopy (XPS) (Figures 6c–e and S26–28). The F 1s and N 1s spectra of *in situ*-SL2 revealed significantly higher concentrations of LiF and Li₃N derived from the AGG structures. With Ar⁺ ion sputtering, the *in situ*-SL2 SPE exhibits a more uniform and deeper distribution of inorganic LiF and Li₃N, with only a minimal presence of Li₂CO₃ at the surface.⁶⁵ The abundant Li₃N, known for its superior ionic conductivity, supports efficient ion transport within the SEI, while LiF mitigates dendrite formation by promoting uniform lithium nucleation.⁶⁶

TOF-SIMS analysis further confirms that introducing trace amounts of SL into the SPEs promotes the formation of a robust SEI layer.^{67,68} As shown in the 3D rendering image from top-down deep sputtering (Figures 6f and S29), the SEI layer from the cycled LFP|*In situ*-SL2|Li cell contains a much deeper distribution of LiF⁻, while only a small amount of organic compounds such as CHO²⁻, and CO₃²⁻ were present on the surface. In contrast, the *in situ*-SL3-based SEI exhibits a higher proportion of organic species and a shallower LiF distribution. Additionally, finite-element method simulations (FEMSS) using COMSOL Multiphysics further quantified the interfacial stability.⁶⁹ As illustrated in Figure 6g, h, *in situ*-SL2 SPE exhibited smaller concentration gradients of Li⁺ during plating and stripping compared to *in situ*-SL3 SPE. Overall, the high *t*_{Li⁺} and the rapid ion transport mechanisms in *in situ*-SL2 SPE mitigate lithium-ion accumulation, effectively altering the electric field distribution and preventing dendrite growth, contributing to the superior electrochemical performance and long-term stability in high-voltage lithium metal batteries.

3. CONCLUSIONS

In this study, we have successfully developed an *in situ*-SL2 SPE by purposely incorporating trace amounts of SL into a polyacrylic-based matrix to construct efficient and adaptable Li⁺ transport pathways in SPEs. This strategy precisely tunes the local solvation environments *via* gradient ion–dipole interactions to establish a dense, multipoint coordination network. Crucially, the inherent flexible conformation of SL, facilitated by its low pseudorotation energy barrier, enables rapid conformational changes and a variable bridging effect. This behavior promotes the creation of “dynamic ion transport

channels,” significantly lowering the energy barriers for Li⁺ hopping and enhancing both ionic conductivity and lithium-ion transference numbers. Further interfacial analyses reveal that the *in situ*-SL2 SPE facilitates the formation of an anion-derived stable, inorganic-rich SEI, enhancing the ionic conductivity and mitigating metal dendrite formation. It also promotes the construction of a stable LiF and Li₂SO₄-enriched CEI, contributing synergistically to improving the high-voltage oxidative stability, suppressing side reactions, and enhancing interface compatibility. Accordingly, the LFP|*In situ*-SL2|Li cell shows over 91.7% capacity retention after 2000 cycles at 3 C, underscoring the long-term stability of the electrolyte. Looking forward, this molecular design strategy can be extended to diverse SPEs by selecting small molecules with tunable dipole moments and flexible conformations, enabling customizable solvation structures and dynamic ion transport pathways for high-performance solid-state batteries.

■ ASSOCIATED CONTENT

SI Supporting Information

The Supporting Information is available free of charge at <https://pubs.acs.org/doi/10.1021/jacs.5c05911>.

Experimental details; includes physical characterizations of the prepared SPEs such as SEM images; elemental mapping images; GPC profile and Raman spectra; electrochemical and battery performance data including CCD profiles; CV curves; EIS data and cycling performance; atomistic molecular dynamics simulations details; provides a deeper understanding of ion transport mechanisms and coordination behavior in the SPE system (Figures S1–S29 and Tables S1,S2) (PDF)

■ AUTHOR INFORMATION

Corresponding Author

Haimei Wang – Department of Materials Science and Engineering, National University of Singapore, Singapore 117574, Republic of Singapore; National Engineering Research Center for Colloidal Materials, School of Chemistry and Chemical Engineering, Shandong University, Jinan, Shandong 250100, China;  orcid.org/0000-0003-2787-7454; Email: whm312a@gmail.com

Authors

Qiang Lv – Department of Materials Science and Engineering, National University of Singapore, Singapore 117574, Republic of Singapore

Li-an Li – School of Ocean, Yantai University, Yantai, Shandong 264005, China

Xi Zhang – China University of Geosciences (Beijing), Beijing Municipality 100083, China

Runqi Wang – National Engineering Research Center for Colloidal Materials, School of Chemistry and Chemical Engineering, Shandong University, Jinan, Shandong 250100, China

Ning Wen – National Engineering Research Center for Colloidal Materials, School of Chemistry and Chemical Engineering, Shandong University, Jinan, Shandong 250100, China

Lijuan Xue – School of Physics and Electrical Engineering, Linyi University, Linyi 276000, China; Department of Physics, City University of Hong Kong, Hong Kong SAR, Kowloon 999077, China

Lei Shen — Department of Mechanical Engineering, National University of Singapore, Singapore 117575, Republic of Singapore; National University of Singapore (Chongqing) Research Institute, Chongqing 401120, China; orcid.org/0000-0001-6198-5753

Dairong Chen — National Engineering Research Center for Colloidal Materials, School of Chemistry and Chemical Engineering, Shandong University, Jinan, Shandong 250100, China; orcid.org/0000-0001-6961-9328

Francesco Ciucci — University of Bayreuth, Chair of Electrode Design for Electrochemical Energy Systems, 95448 Bayreuth, Germany; University of Bayreuth, Bavarian Center for Battery Technology (BayBatt), 95447 Bayreuth, Germany; orcid.org/0000-0003-0614-5537

John Wang — Department of Materials Science and Engineering, National University of Singapore, Singapore 117574, Republic of Singapore; National University of Singapore (Chongqing) Research Institute, Chongqing 401120, China; orcid.org/0000-0001-6059-8962

Complete contact information is available at:
<https://pubs.acs.org/10.1021/jacs.5c05911>

Author Contributions

All authors contributed to the overall scientific interpretation and edited the manuscript.

Notes

The authors declare no competing financial interest.

ACKNOWLEDGMENTS

This work was supported by Singapore NRF (NRF-CRP26-2021-0003), Ministry of Education, Singapore, Tier 2 (project No. A-8001872-00-00), the National Natural Science Foundation of China (Grant 22275116), and the Natural Science Foundation of Shandong Province (ZR2023QB207); this research work was conducted at the Shandong University and the National University of Singapore.

REFERENCES

- (1) Li, X.; Kim, J. T.; Luo, J.; Zhao, C.; Xu, Y.; Mei, T.; Li, R.; Liang, J.; Sun, X. Structural Regulation of Halide Superionic Conductors for All-Solid-State Lithium Batteries. *Nat. Commun.* **2024**, *15* (1), No. 53.
- (2) Wang, C.; Liang, J.; Zhao, Y.; Zheng, M.; Li, X.; Sun, X. All-Solid-State Lithium Batteries Enabled by Sulfide Electrolytes: From Fundamental Research to Practical Engineering Design. *Energy Environ. Sci.* **2021**, *14* (5), 2577–2619.
- (3) Yang, X.; Adair, K. R.; Gao, X.; Sun, X. Recent Advances and Perspectives on Thin Electrolytes for High-Energy-Density Solid-State Lithium Batteries. *Energy Environ. Sci.* **2021**, *14* (2), 643–671.
- (4) Zhao, P.; Wang, Y.; Huang, Q.; Jin, Z.; Li, C. Metal–Organic Coordination Enhanced Metallocopolymer Electrolytes for Wide-Temperature Solid-State Lithium Metal Batteries. *Angew. Chem., Int. Ed.* **2025**, *64* (5), No. e202416897.
- (5) Liang, W.; Zhou, X.; Zhang, B.; Zhao, Z.; Song, X.; Chen, K.; Wang, L.; Ma, Z.; Liu, J. The Versatile Establishment of Charge Storage in Polymer Solid Electrolyte with Enhanced Charge Transfer for LiF-Rich SEI Generation in Lithium Metal Batteries. *Angew. Chem., Int. Ed.* **2024**, *63* (18), No. e202320149.
- (6) Liu, W.; Yi, C.; Li, L.; Liu, S.; Gui, Q.; Ba, D.; Li, Y.; Peng, D.; Liu, J. Designing Polymer-in-Salt Electrolyte and Fully Infiltrated 3D Electrode for Integrated Solid-State Lithium Batteries. *Angew. Chem., Int. Ed.* **2021**, *60* (23), 12931–12940.
- (7) Zhu, J.; Zhang, Z.; Zhao, S.; Westover, A. S.; Belharouak, I.; Cao, P. Single-Ion Conducting Polymer Electrolytes for Solid-State Lithium–Metal Batteries: Design, Performance, and Challenges. *Adv. Energy Mater.* **2021**, *11* (14), No. 2003836.
- (8) Armand, M.; Gruegeon, S.; Castresana, K. G.; Del Amo, J. M. L.; Bonilla, F.; Cid, R.; Laruelle, S.; Devaraj, S. Poly(Vinyl Butyrate) Esters as Stable Polymer Matrix for Solid-State Li-Metal Batteries. *ACS Energy Lett.* **2025**, *10* (1), 579–587.
- (9) Ye, G.; Zhu, L.; Ma, Y.; He, M.; Zheng, C.; Shen, K.; Hong, X.; Xiao, Z.; Jia, Y.; Gao, P.; Pang, Q. Molecular Design of Solid Polymer Electrolytes with Enthalpy–Entropy Manipulation for Li Metal Batteries with Aggressive Cathode Chemistry. *J. Am. Chem. Soc.* **2024**, *146* (40), 27668–27678.
- (10) Ding, P.; Lin, Z.; Guo, X.; Wu, L.; Wang, Y.; Guo, H.; Li, L.; Yu, H. Polymer Electrolytes and Interfaces in Solid-State Lithium Metal Batteries. *Mater. Today* **2021**, *51*, 449–474.
- (11) Liu, S.; Liu, W.; Ba, D.; Zhao, Y.; Ye, Y.; Li, Y.; Liu, J. Filler-Integrated Composite Polymer Electrolyte for Solid-State Lithium Batteries. *Adv. Mater.* **2023**, *35* (2), No. 2110423.
- (12) Lu, G.; Niu, J.; Du, X.; Liu, C.; Xing, M.; Chao, D.; He, Y.; Ma, L.; Liu, Z.; Zhao, J.; Zhang, Y.; Cui, G. Eutectic Perturbations Enhance Multivalent-Cation Structural Diffusion in Salt-Concentrated Polymer Electrolytes. *ACS Energy Lett.* **2025**, *10* (1), 296–304.
- (13) Liu, J.; Wu, Z.; Stadler, F. J.; Huang, Y. High Dielectric Poly(Vinylidene Fluoride)-Based Polymer Enables Uniform Lithium-Ion Transport in Solid-State Ionogel Electrolytes. *Angew. Chem., Int. Ed.* **2023**, *62* (26), No. e202300243.
- (14) Zhao, Y.; Wang, L.; Zhou, Y.; Liang, Z.; Tavajohi, N.; Li, B.; Li, T. Solid Polymer Electrolytes with High Conductivity and Transference Number of Li Ions for Li-Based Rechargeable Batteries. *Adv. Sci.* **2021**, *8* (7), No. 2003675.
- (15) Pan, J.; Zhao, P.; Wang, N.; Huang, F.; Dou, S. Research Progress in Stable Interfacial Constructions between Composite Polymer Electrolytes and Electrodes. *Energy Environ. Sci.* **2022**, *15* (7), 2753–2775.
- (16) Xu, S.; Xu, R.; Yu, T.; Chen, K.; Sun, C.; Hu, G.; Bai, S.; Cheng, H.-M.; Sun, Z.; Li, F. Decoupling of Ion Pairing and Ion Conduction in Ultrahigh-Concentration Electrolytes Enables Wide-Temperature Solid-State Batteries. *Energy Environ. Sci.* **2022**, *15* (8), 3379–3387.
- (17) Yang, W.; Liu, Y.; Sun, X.; He, Z.; He, P.; Zhou, H. Solvation-Tailored PVDF-Based Solid-State Electrolyte for High-Voltage Lithium Metal Batteries. *Angew. Chem., Int. Ed.* **2024**, *63* (18), No. e202401428.
- (18) Liu, Q.; Yang, G.; Li, X.; Zhang, S.; Chen, R.; Wang, X.; Gao, Y.; Wang, Z.; Chen, L. Polymer Electrolytes Based on Interactions between [Solvent-Li⁺] Complex and Solvent-Modified Polymer. *Energy Storage Mater.* **2022**, *51*, 443–452.
- (19) Li, M.; An, H.; Song, Y.; Liu, Q.; Wang, J.; Huo, H.; Lou, S.; Wang, J. Ion–Dipole-Interaction-Induced Encapsulation of Free Residual Solvent for Long-Cycle Solid-State Lithium Metal Batteries. *J. Am. Chem. Soc.* **2023**, *145* (47), 25632–25642.
- (20) Wang, Z.; Chen, J.; Fu, J.; Li, Z.; Guo, X. Polymer-Based Electrolytes for High-Voltage Solid-State Lithium Batteries. *Energy Mater.* **2024**, *4* (4), No. 400050.
- (21) Song, Z.; Chen, F.; Martínez-Ibañez, M.; Feng, W.; Forsyth, M.; Zhou, Z.; Armand, M.; Zhang, H. A Reflection on Polymer Electrolytes for Solid-State Lithium Metal Batteries. *Nat. Commun.* **2023**, *14* (1), No. 4884.
- (22) Wen, K.; Xin, C.; Guan, S.; Wu, X.; He, S.; Xue, C.; Liu, S.; Shen, Y.; Li, L.; Nan, C. Ion–Dipole Interaction Regulation Enables High-Performance Single-Ion Polymer Conductors for Solid-State Batteries. *Adv. Mater.* **2022**, *34* (32), No. 2202143.
- (23) Yan, S.; Liu, H.; Lu, Y.; Feng, Q.; Zhou, H.; Wu, Y.; Hou, W.; Xia, Y.; Zhou, H.; Zhou, P.; Song, X.; Ou, Y.; Liu, K. Selectively Fluorinated Aromatic Lithium Salts Regulate the Solvation Structure and Interfacial Chemistry for All-Solid-State Batteries. *Sci. Adv.* **2025**, *11* (5), No. eads4014.
- (24) Mu, K.; Wang, D.; Dong, W.; Liu, Q.; Song, Z.; Xu, W.; Yao, P.; Chen, Y.; Yang, B.; Li, C.; Tian, L.; Zhu, C.; Xu, J. Hybrid Crosslinked Solid Polymer Electrolyte via In-Situ Solidification Enables High-

- Performance Solid-State Lithium Metal Batteries. *Adv. Mater.* **2023**, *35* (47), No. 2304686.
- (25) Qi, S.; Li, M.; Gao, Y.; Zhang, W.; Liu, S.; Zhao, J.; Du, L. Enabling Scalable Polymer Electrolyte with Dual-Reinforced Stable Interface for 4.5 V Lithium-Metal Batteries. *Adv. Mater.* **2023**, *35* (45), No. 2304951.
- (26) Lv, Q.; Song, Y.; Wang, B.; Wang, S.; Wu, B.; Jing, Y.; Ren, H.; Yang, S.; Wang, L.; Xiao, L.; Wang, D.; Liu, H.; Dou, S. Bifunctional Flame Retardant Solid-State Electrolyte toward Safe Li Metal Batteries. *J. Energy Chem.* **2023**, *81*, 613–622.
- (27) Hou, Y.; Huang, Z.; Chen, Z.; Li, X.; Chen, A.; Li, P.; Wang, Y.; Zhi, C. Bifunctional Separators Design for Safe Lithium-Ion Batteries: Suppressed Lithium Dendrites and Fire Retardance. *Nano Energy* **2022**, *97*, No. 107204.
- (28) Chen, T.-L.; Liu, M.; Fan, X.-Y.; Feng, Y.-H.; Liu, Q.; Liu, X.-R.; Xin, H.; Wang, P.-F. Nonflammable Sulfone-Based Electrolytes with Mechanically and Thermally Stable Interfaces Enabling $\text{LiNi}_{0.5}\text{Mn}_{1.5}\text{O}_4$ to Operate at High Temperature. *ACS Energy Lett.* **2024**, *9* (11), 5452–5460.
- (29) Chen, K.; Shen, X.; Luo, L.; Chen, H.; Cao, R.; Feng, X.; Chen, W.; Fang, Y.; Cao, Y. Correlating the Solvating Power of Solvents with the Strength of Ion-Dipole Interaction in Electrolytes of Lithium-ion Batteries. *Angew. Chem., Int. Ed.* **2023**, *62* (47), No. e202312373.
- (30) Zhou, H.; Ou, Y.; Yan, S.; Xie, J.; Zhou, P.; Wan, L.; Xu, Z.; Liu, F.; Zhang, W.; Xia, Y.; Liu, K. Supramolecular Polymer Ion Conductor with Weakened Li Ion Solvation Enables Room Temperature All-Solid-State Lithium Metal Batteries. *Angew. Chem., Int. Ed.* **2023**, *62* (35), No. e202306948.
- (31) Dokko, K.; Watanabe, D.; Ugata, Y.; Thomas, M. L.; Tsuzuki, S.; Shinoda, W.; Hashimoto, K.; Ueno, K.; Umebayashi, Y.; Watanabe, M. Direct Evidence for Li Ion Hopping Conduction in Highly Concentrated Sulfolane-Based Liquid Electrolytes. *J. Phys. Chem. B* **2018**, *122* (47), 10736–10745.
- (32) Da, X.; Chen, J.; Qin, Y.; Zhao, J.; Jia, X.; Zhao, Y.; Deng, X.; Li, Y.; Gao, N.; Su, Y.; Rong, Q.; Kong, X.; Xiong, J.; Hu, X.; Ding, S.; Gao, G. CO_2 -Assisted Induced Self-Assembled Aramid Nanofiber Aerogel Composite Solid Polymer Electrolyte for All-Solid-State Lithium-Metal Batteries. *Adv. Energy Mater.* **2024**, *14* (11), No. 2303527.
- (33) Tang, F.; Wang, L.; Huang, X.; Yin, X.; Tian, Y.; Wang, Z.; Cui, X.; Xu, Q. Pendulum-Swing Coordination Boosting “Liquid-like” Li-Ion Conduction within Asymmetric Lamellar Fillers for Solid Polymer Electrolytes. *Chem. Eng. J.* **2024**, *482*, No. 148995.
- (34) Han, S.; Wen, P.; Wang, H.; Zhou, Y.; Gu, Y.; Zhang, L.; Shao-Horn, Y.; Lin, X.; Chen, M. Sequencing Polymers to Enable Solid-State Lithium Batteries. *Nat. Mater.* **2023**, *22* (12), 1515–1522.
- (35) Wu, J.; Gao, Z.; Wang, Y.; Yang, X.; Liu, Q.; Zhou, D.; Wang, X.; Kang, F.; Li, B. Electrostatic Interaction Tailored Anion-Rich Solvation Sheath Stabilizing High-Voltage Lithium Metal Batteries. *Nano-Micro Lett.* **2022**, *14* (1), No. 147.
- (36) Hou, J.; Xie, W.; Shang, L.; Wu, S.; Cui, Y.; Li, Y.; Yan, Z.; Zhang, K.; Lu, Y.; Chen, J. Nanocrystals with Aggregate Anionic Structure Enable Ion Transport Decoupling of Chain Segment Movement in Poly(Ethylene Oxide) Electrolytes. *Angew. Chem., Int. Ed.* **2025**, *64*, No. e202418783.
- (37) Zhang, Y.; Liu, H.; Liu, F.; Zhang, S.; Zhou, M.; Liao, Y.; Wei, Y.; Dong, W.; Li, T.; Liu, C.; Liu, Q.; Xu, H.; Sun, G.; Wang, Z.; Ren, Y.; Yang, J. Dual-Anion-Rich Polymer Electrolytes for High-Voltage Solid-State Lithium Metal Batteries. *ACS Nano* **2025**, *19* (3), 3197–3209.
- (38) Shi, J.; Xu, C.; Lai, J.; Li, Z.; Zhang, Y.; Liu, Y.; Ding, K.; Cai, Y.; Shang, R.; Zheng, Q. An Amphiphilic Molecule-Regulated Core-Shell-Solvation Electrolyte for Li-Metal Batteries at Ultra-Low Temperature. *Angew. Chem.* **2023**, *135* (13), No. e202218151.
- (39) He, Y.; Shan, X.; Li, Y.; Li, Z.; Li, L.; Zhao, S.; Gao, S.; Qu, J.; Yang, H.; Cao, P.-F. In-Situ Formation of Quasi-Solid Polymer Electrolyte for Wide-Temperature Applicable Li-Metal Batteries. *Energy Storage Mater.* **2024**, *68*, No. 103281.
- (40) Zhao, L.; Dong, Q.; Wang, Y.; Xue, G.; Wang, X.; Li, Z.; Shao, H.; Chen, H.; Shen, Y.; Chen, L. Anion Modulation: Enabling Highly Conductive Stable Polymer Electrolytes for Solid-State Li-Metal Batteries. *Angew. Chem., Int. Ed.* **2024**, *63* (52), No. e202412280.
- (41) Jin, Y.; Lin, R.; Li, Y.; Zhang, X.; Tan, S.; Shuai, Y.; Xiong, Y. Revealing the Influence of Electron Migration Inside Polymer Electrolyte on Li^+ Transport and Interphase Reconfiguration for Li Metal Batteries. *Angew. Chem., Int. Ed.* **2024**, *63* (24), No. e202403661.
- (42) Zhao, Y.; Li, L.; Zhou, D.; Ma, Y.; Zhang, Y.; Yang, H.; Fan, S.; Tong, H.; Li, S.; Qu, W. Opening and Constructing Stable Lithium-Ion Channels within Polymer Electrolytes. *Angew. Chem., Int. Ed.* **2024**, *63* (31), No. e202404728.
- (43) Wang, T.; Yuan, H.; Wang, H.; Guo, Y.; Yang, J.; Liu, X.; Liu, B.; Wang, X.; Kirk, C. H.; Sun, J.; Zhang, Y.; Wang, J. Unlocking Fast Ionic Transport in Sub-Nano Channels of MOF-Based Electrolytes for Next-Generation Batteries. *Adv. Funct. Mater.* **2024**, *34* (45), No. 2405699.
- (44) Atik, J.; Diddens, D.; Thienenkamp, J. H.; Brunklaus, G.; Winter, M.; Paillard, E. Cation-Assisted Lithium-Ion Transport for High-Performance PEO-based Ternary Solid Polymer Electrolytes. *Angew. Chem., Int. Ed.* **2021**, *60* (21), 11919–11927.
- (45) Xu, H.; Yang, J.; Niu, Y.; Hou, X.; Sun, Z.; Jiang, C.; Xiao, Y.; He, C.; Yang, S.; Li, B.; Chen, W. Deciphering and Integrating Functionalized Side Chains for High Ion-Conductive Elastic Ternary Copolymer Solid-State Electrolytes for Safe Lithium Metal Batteries. *Angew. Chem., Int. Ed.* **2024**, *63* (36), No. e202406637.
- (46) Huang, X.; Li, R.; Sun, C.; Zhang, H.; Zhang, S.; Lv, L.; Huang, Y.; Fan, L.; Chen, L.; Noked, M.; Fan, X. Solvent-Assisted Hopping Mechanism Enables Ultrafast Charging of Lithium-Ion Batteries. *ACS Energy Lett.* **2022**, *7* (11), 3947–3957.
- (47) Ikeda, S.; Tsuzuki, S.; Sudoh, T.; Shigenobu, K.; Ueno, K.; Dokko, K.; Watanabe, M.; Shinoda, W. Lithium-Ion Dynamics in Sulfolane-Based Highly Concentrated Electrolytes. *J. Phys. Chem. C* **2023**, *127* (28), 13837–13845.
- (48) Han, K. S.; Bazak, J. D.; Chen, Y.; Graham, T. R.; Washiton, N. M.; Hu, J. Z.; Murugesan, V.; Mueller, K. T. Pulsed Field Gradient Nuclear Magnetic Resonance and Diffusion Analysis in Battery Research. *Chem. Mater.* **2021**, *33* (22), 8562–8590.
- (49) Cheng, Y.; Liu, X.; Guo, Y.; Dong, G.; Hu, X.; Zhang, H.; Xiao, X.; Liu, Q.; Xu, L.; Mai, L. Monodispersed Sub-1 nm Inorganic Cluster Chains in Polymers for Solid Electrolytes with Enhanced Li-Ion Transport. *Adv. Mater.* **2023**, *35* (47), No. 2303226.
- (50) Bocharova, V.; Sokolov, A. P. Perspectives for Polymer Electrolytes: A View from Fundamentals of Ionic Conductivity. *Macromolecules* **2020**, *53* (11), 4141–4157.
- (51) Li, R.; Hua, H.; Yang, X.; Tian, J.; Chen, Q.; Huang, R.; Li, X.; Zhang, P.; Zhao, J. The Deconstruction of a Polymeric Solvation Cage: A Critical Promotion Strategy for PEO-Based All-Solid Polymer Electrolytes. *Energy Environ. Sci.* **2024**, *17* (15), 5601–5612.
- (52) Lu, D.; Li, R.; Rahman, M. M.; Yu, P.; Lv, L.; Yang, S.; Huang, Y.; Sun, C.; Zhang, S.; Zhang, H.; Zhang, J.; Xiao, X.; Deng, T.; Fan, L.; Chen, L.; Wang, J.; Hu, E.; Wang, C.; Fan, X. Ligand-Channel-Enabled Ultrafast Li-Ion Conduction. *Nature* **2024**, *627* (8002), 101–107.
- (53) Ma, Y.; Wan, J.; Yang, Y.; Ye, Y.; Xiao, X.; Boyle, D. T.; Burke, W.; Huang, Z.; Chen, H.; Cui, Y.; Yu, Z.; Oyakhire, S. T.; Cui, Y. Scalable, Ultrathin, and High-Temperature-Resistant Solid Polymer Electrolytes for Energy-Dense Lithium Metal Batteries. *Adv. Energy Mater.* **2022**, *12* (15), No. 2103720.
- (54) Wang, Y.; Chen, S.; Li, Z.; Peng, C.; Li, Y.; Feng, W. In-Situ Generation of Fluorinated Polycarbonate Copolymer Solid Electrolytes for High-Voltage Li-Metal Batteries. *Energy Storage Mater.* **2022**, *45*, 474–483.
- (55) Wang, S.; Lv, Q.; Jing, Y.; Wang, B.; Wang, D.; Liu, H.; Dou, S. In Situ Polymerization Design of a Quasi-Solid Electrolyte Enhanced by NMP Additive for Lithium Metal Batteries. *Energy Storage Mater.* **2024**, *69*, No. 103390.

- (56) Liu, Y.; Hu, R.; Zhang, D.; Liu, J.; Liu, F.; Cui, J.; Lin, Z.; Wu, J.; Zhu, M. Constructing Li-Rich Artificial SEI Layer in Alloy-Polymer Composite Electrolyte to Achieve High Ionic Conductivity for All-Solid-State Lithium Metal Batteries. *Adv. Mater.* **2021**, *33* (11), No. 2004711.
- (57) Qin, S.; Yu, Y.; Zhang, J.; Ren, Y.; Sun, C.; Zhang, S.; Zhang, L.; Hu, W.; Yang, H.; Yang, D. Separator-Free In Situ Dual-Curing Solid Polymer Electrolytes with Enhanced Interfacial Contact for Achieving Ultrastable Lithium-Metal Batteries. *Adv. Energy Mater.* **2023**, *13* (34), No. 2301470.
- (58) Zhang, W.; Koverga, V.; Liu, S.; Zhou, J.; Wang, J.; Bai, P.; Tan, S.; Dandu, N. K.; Wang, Z.; Chen, F.; Xia, J.; Wan, H.; Zhang, X.; Yang, H.; Lucht, B. L.; Li, A.-M.; Yang, X.-Q.; Hu, E.; Raghavan, S. R.; Ngo, A. T.; Wang, C. Single-Phase Local-High-Concentration Solid Polymer Electrolytes for Lithium-Metal Batteries. *Nat. Energy* **2024**, *9* (4), 386–400.
- (59) Liu, Y.; Jin, Z.; Liu, Z.; Xu, H.; Sun, F.; Zhang, X.; Chen, T.; Wang, C. Regulating the Solvation Structure in Polymer Electrolytes for High-Voltage Lithium Metal Batteries. *Angew. Chem., Int. Ed.* **2024**, *63* (34), No. e202405802.
- (60) Yang, H.; Zhang, B.; Jing, M.; Shen, X.; Wang, L.; Xu, H.; Yan, X.; He, X. In Situ Catalytic Polymerization of a Highly Homogeneous PDOL Composite Electrolyte for Long-Cycle High-Voltage Solid-State Lithium Batteries. *Adv. Energy Mater.* **2022**, *12* (39), No. 2201762.
- (61) Adenusi, H.; Chass, G. A.; Passerini, S.; Tian, K. V.; Chen, G. Lithium Batteries and the Solid Electrolyte Interphase (SEI)—Progress and Outlook. *Adv. Energy Mater.* **2023**, *13* (10), No. 2203307.
- (62) Lv, Q.; Li, C.; Liu, Y.; Jing, Y.; Sun, J.; Wang, H.; Wang, L.; Ren, H.; Wu, B.; Cheng, T.; Wang, D.; Liu, H.; Dou, S.-X.; Wang, B.; Wang, J. In-Situ Polymerized High-Voltage Solid-State Lithium Metal Batteries with Dual-Reinforced Stable Interfaces. *ACS Nano* **2024**, *18* (34), 23253–23264.
- (63) Li, Y.; Wen, B.; Li, N.; Zhao, Y.; Chen, Y.; Yin, X.; Da, X.; Ouyang, Y.; Li, X.; Kong, P.; Ding, S.; Xi, K.; Gao, G. Electrolyte Engineering to Construct Robust Interphase with High Ionic Conductivity for Wide Temperature Range Lithium Metal Batteries. *Angew. Chem., Int. Ed.* **2025**, *64* (2), No. e202414636.
- (64) Chen, Y.; Li, M.; Liu, Y.; Jie, Y.; Li, W.; Huang, F.; Li, X.; He, Z.; Ren, X.; Chen, Y.; Meng, X.; Cheng, T.; Gu, M.; Jiao, S.; Cao, R. Origin of Dendrite-Free Lithium Deposition in Concentrated Electrolytes. *Nat. Commun.* **2023**, *14* (1), No. 2655.
- (65) Wei, Y.; Wang, H.; Lin, X.; Wang, T.; Cui, Y.; Huang, Y.; Yang, J.; Liu, T.-H.; Ren, Y.; Fan, X.; Xu, H.; Huang, Y. Moderate Solvation Structures of Lithium Ions for High-Voltage Lithium Metal Batteries at -40°C . *Energy Environ. Sci.* **2025**, *18* (2), 786–798.
- (66) Wu, Q.; Fang, M.; Jiao, S.; Li, S.; Zhang, S.; Shen, Z.; Mao, S.; Mao, J.; Zhang, J.; Tan, Y.; Shen, K.; Lv, J.; Hu, W.; He, Y.; Lu, Y. Phase Regulation Enabling Dense Polymer-Based Composite Electrolytes for Solid-State Lithium Metal Batteries. *Nat. Commun.* **2023**, *14* (1), No. 6296.
- (67) Xu, P.; Gao, Y.; Huang, Y.; Shuang, Z.; Kong, W.; Huang, X.; Huang, W.; Yao, N.; Chen, X.; Yuan, H.; Zhao, C.; Huang, J.; Zhang, Q. Solvation Regulation Reinforces Anion-Derived Inorganic-Rich Interphase for High-Performance Quasi-Solid-State Li Metal Batteries. *Adv. Mater.* **2024**, *36* (44), No. 2409489.
- (68) Wang, Z.; Zhao, C.; Yao, N.; Lu, Y.; Xue, Z.; Huang, X.; Xu, P.; Huang, W.; Wang, Z.; Huang, J.; Zhang, Q. The Regulation of Solid Electrolyte Interphase on Composite Lithium Anodes in Solid-State Batteries. *Angew. Chem., Int. Ed.* **2025**, *64* (2), No. e202414524.
- (69) Su, Y.; Rong, X.; Li, H.; Huang, X.; Chen, L.; Liu, B.; Hu, Y. High-Entropy Microdomain Interlocking Polymer Electrolytes for Advanced All-Solid-State Battery Chemistries. *Adv. Mater.* **2023**, *35* (1), No. 2209402.

■ NOTE ADDED AFTER ASAP PUBLICATION

This paper was published on July 15, 2025. Figures 2 and 4 were updated. The corrected version was reposted on July 28, 2025.



CAS INSIGHTS™

EXPLORE THE INNOVATIONS SHAPING TOMORROW

Discover the latest scientific research and trends with CAS Insights. Subscribe for email updates on new articles, reports, and webinars at the intersection of science and innovation.

Subscribe today

CAS
A division of the
American Chemical Society